

Direct measurements of the extraordinary optical momentum and transverse spin-dependent force using a nano-cantilever

M. Antognozzi^{1,2*}, C. R. Bermingham¹, R. Harniman^{1,3}, S. Simpson^{1,4}, J. Senior¹, R. Hayward¹, H. Hoerber¹, M. R. Dennis¹, A. Y. Bekshaev⁵, K. Y. Bliokh^{6,7*}, and F. Nori^{6,8}

¹*H.H. Wills Physics Laboratory, University of Bristol, Bristol BS8 1TL, UK*

²*Centre for Nanoscience and Quantum Information, University of Bristol, Bristol, UK*

³*School of Chemistry, University of Bristol, Bristol BS8 1TL, UK*

⁴*Institute of Scientific Instruments of the ASCR, Brno, Czech Republic*

⁵*I.I. Mechnikov National University, Odessa, 65082 Ukraine*

⁶*Center for Emergent Matter Science, RIKEN, Wako-shi, Saitama 351-0198, Japan*

⁷*Nonlinear Physics Centre, RSPE, The Australian National University, Canberra, Australia*

⁸*Physics Department, University of Michigan, Ann Arbor, Michigan 48109-1040, USA*

*e-mail: Massimo.Antognozzi@bristol.ac.uk, k.bliokh@gmail.com

1. Calculations of the fields and momentum densities

1.1. Canonical and spin momenta: from relativistic field theory to optical fields

The canonical energy-momentum tensor for the free-space Maxwell field follows from the space-time translation symmetry of the field Lagrangian and Noether's theorem [10]. Using standard relativistic notation with the Einstein summation rule, the canonical energy-momentum tensor reads

$$T_{\text{can}}^{\alpha\beta} = (\partial^\alpha A_\gamma) F^{\beta\gamma} - \frac{1}{4} g^{\alpha\beta} F^{\gamma\delta} F_{\gamma\delta}, \quad (\text{S1})$$

where A^α is the electromagnetic four-potential, $F^{\alpha\beta}$ is the field tensor, and $g^{\alpha\beta}$ is the Minkowski spacetime metric tensor. The tensor (S1) is gauge-dependent (due to the presence of A^α) and non-symmetric. Nonetheless, it is this tensor that corresponds to the generators of spatial translations for the electromagnetic field.

In 1940, Belinfante suggested a symmetrisation procedure to “improve” tensor (S1), i.e., to make it gauge-invariant and symmetric [9,10]. He added the following total-divergence term (constructed from the spin tensor) to the canonical energy-momentum tensor:

$$T_{\text{spin}}^{\alpha\beta} = -\partial_\gamma (A^\alpha F^{\beta\gamma}), \quad (\text{S2})$$

The resulting symmetric energy-momentum tensor (also known as the Belinfante energy-momentum tensor) is

$$\mathcal{T}^{\alpha\beta} = T_{\text{can}}^{\alpha\beta} + T_{\text{spin}}^{\alpha\beta} = F^\alpha_\gamma F^{\beta\gamma} - \frac{1}{4} g^{\alpha\beta} F^{\gamma\delta} F_{\gamma\delta}. \quad (\text{S3})$$

This tensor (S3) is typically considered as meaningful in field theory, because it is gauge-invariant and is naturally coupled to gravity [10]. In turn, the Belinfante spin-correction term (S2) is usually regarded as “virtual”, because it does not contribute to the energy-momentum conservation law, energy transport, and integral momentum of a localized field [10,11,15].

The momentum density of a free electromagnetic field is given by the $T^{i0} \equiv P^i$ components of the energy-momentum tensor. In this manner, the canonical, spin, and Poynting momentum densities are obtained from Eqs. (S1)–(S3) as

$$\mathbf{P}^{\text{can}} = \mathbf{E} \cdot (\nabla) \mathbf{A}, \quad \mathbf{P}^{\text{spin}} = -(\mathbf{E} \cdot \nabla) \mathbf{A}, \quad \mathcal{P} = \mathbf{P}^{\text{can}} + \mathbf{P}^{\text{spin}} = \mathbf{E} \times \mathbf{B}, \quad (\text{S4})$$

where \mathbf{E} and \mathbf{B} are the electric and magnetic fields, whereas \mathbf{A} is the vector-potential. Note that in Eqs. (S4) and in what follows we use Berry’s notation $\mathbf{X} \cdot (\nabla) \mathbf{Y} \equiv X_i \nabla Y_i$ [13] and natural electro-dynamical units $\epsilon_0 = \mu_0 = c = 1$.

Although the canonical and spin momenta are gauge-dependent, there are several strong indications that in a number of situations the *experimentally-measured quantities correspond to the canonical quantities taken in some particular gauge*. Recently, this was actively discussed in relation to optical experiments with laser fields [7,8,14,15,22,23,25,S1–S6] and QED experiments detecting gluon and quark spin and orbital contributions to the proton spin [26]. In optical experiments, the measured quantities correspond to the *Coulomb gauge*, i.e., $A^0 = 0$ and $\nabla \cdot \mathbf{A} = 0$, and hereafter we assume this gauge.

We are interested in *monochromatic* optical fields, which can be described by complex time-independent field amplitudes: $\mathbf{E}(\mathbf{r}, t) \rightarrow \text{Re}[\mathbf{E}(\mathbf{r})e^{-i\omega t}]$, $\mathbf{B}(\mathbf{r}, t) \rightarrow \text{Re}[\mathbf{B}(\mathbf{r})e^{-i\omega t}]$, $\mathbf{A}(\mathbf{r}, t) \rightarrow \text{Re}[\mathbf{A}(\mathbf{r})e^{-i\omega t}]$, where ω is the frequency. Here we use the same letters \mathbf{E} , \mathbf{B} , and \mathbf{A} for the complex field amplitudes, and imply only these complex fields in what follows. Importantly, the corresponding vector-potential amplitude (in the Coulomb gauge) becomes simply proportional to the electric field amplitude [15]: $\mathbf{A}(\mathbf{r}) = -i\omega^{-1}\mathbf{E}(\mathbf{r})$. Substituting these equations into Eqs. (S4), and performing *time averaging* over the ω -oscillations, we obtain expressions for the canonical, spin, and Poynting momentum densities in a generic *optical* field [13,15]:

$$\mathbf{P}^{\text{can}} = \frac{1}{2\omega} \text{Im}[\mathbf{E}^* \cdot (\nabla) \mathbf{E}], \quad \mathbf{P}^{\text{spin}} = \frac{1}{4\omega} \nabla \times \text{Im}[\mathbf{E}^* \times \mathbf{E}], \quad \text{Re} \mathcal{P} = \mathbf{P}^{\text{can}} + \mathbf{P}^{\text{spin}} = \frac{1}{2} \text{Re}(\mathbf{E}^* \times \mathbf{B}). \quad (\text{S5})$$

Here we use the same letters \mathbf{P}^{can} , \mathbf{P}^{spin} , and \mathcal{P} for time-averaged optical momenta densities, and consider only these quantities in what follows. Note that for monochromatic fields the Poynting vector is described by a complex quantity $\mathcal{P} = (\mathbf{E}^* \times \mathbf{B})/2$, whose real part corresponds to the usual Poynting momentum (S5), whereas the imaginary part $\text{Im} \mathcal{P}$ describes the “alternating flow of the stored energy” [12].

The canonical momentum in Eqs. (S5) is proportional to the local expectation value of the canonical momentum operator $\hat{\mathbf{p}} = -i\nabla$, and is proportional to the phase gradient or *local wavevector* of the field [13–15,23]:

$$\mathbf{P}^{\text{can}} \propto \text{Re}[\mathbf{E}^* \cdot (\hat{\mathbf{p}}) \mathbf{E}] \propto \mathbf{k}^{\text{loc}} |\mathbf{E}|^2. \quad (\text{S6})$$

In turn, the spin momentum in Eqs. (S5) represents a solenoidal edge current, which is generated by the intrinsic spin angular momentum in the field:

$$\mathbf{P}^{\text{spin}} = \frac{1}{2} \nabla \times \mathbf{S}, \quad \mathbf{S} = \frac{1}{2\omega} \text{Im}[\mathbf{E}^* \times \mathbf{E}] \propto \mathbf{E}^* \cdot (\hat{\mathbf{S}}) \mathbf{E}, \quad (\text{S7})$$

where $\hat{\mathbf{S}}$ is the vector of spin-1 matrices [13,15,S5]. Equations (S5)–(S7) reveal different physical origins and meanings of the two optical momenta constituting the Poynting vector.

Note that throughout this work we use the “standard” formalism for the canonical and spin quantities, which is based on the *electric* field [10,14,15,S3]. There is also a “dual-symmetric” formalism, where all quantities are symmetrized with respect to similar *electric* and *magnetic* field contributions [7,8,13,15,S3–S5,S7]. While the dual-symmetric approach is more natural for free-space fields, in our experiments the probes are sensitive only to the electric field, and, therefore, the standard “electric-biased” formalism is more suitable.

1.2. Fields and momenta in an evanescent optical wave

To calculate the fields and momenta in the evanescent field investigated in our experiment, we need to describe several transformations of the optical field on its way from the laser to the probe (cantilever). The schematic of the experiment is shown in Figures 1 and 2 of the main text, and also in Figure S1.

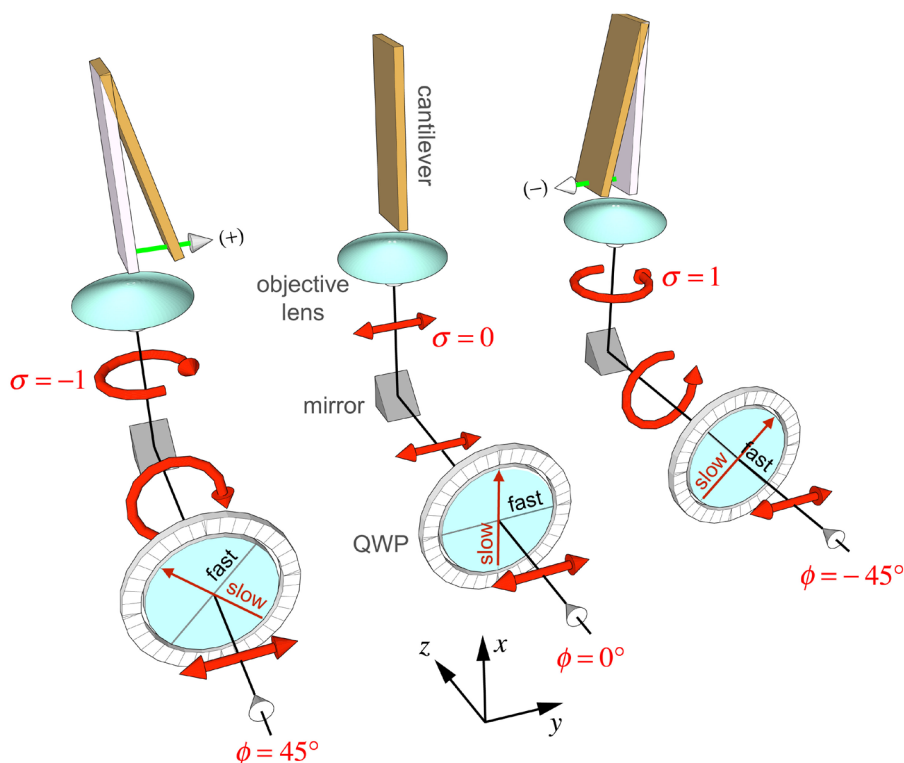


Figure S1. Transformations of the laser 1 beam and its polarization in the experimental setup (see also Fig. 2). Shown are: the coordinate frame (x, y, z) accompanying the beam, rotations of the quarter waveplate (QWP) generating circular polarizations, flip of the circular polarizations after the beam reflection at the mirror, and spin-dependent deflections of the cantilever produced by the transverse force associated with the Belinfante spin momentum.

We describe the complex electric field of the laser-1 beam in its accompanying frame (x, y, z) , where the z -axis is directed along the beam and the y -axis is the transverse (horizontal) axis. Thus, the s and p polarizations correspond to the y and x linear polarizations,

respectively. Neglecting the longitudinal z -component in the paraxial laser field, the laser 1 emits the s -polarized field \mathbf{E}_0 described by the following Jones-vector form:

$$\begin{pmatrix} E_{0,x} \\ E_{0,y} \end{pmatrix} = E_0 \begin{pmatrix} 0 \\ 1 \end{pmatrix} \exp(ikz). \quad (\text{S8})$$

Here E_0 is the electric-field amplitude, and $k = 2\pi/\lambda$ is the wavenumber of the laser 1.

Next, the field (S8) is transmitted through the quarter waveplate (QWP) with its fast axis forming an angle ϕ with the y -axis, as shown in Fig. S1. (We intentionally defined the ϕ angle in the direction opposite to the usual rotations in the (x,y) -plane to account for the flip of the wave helicity in the reflection from the mirror after the QWP.) After the QWP, the slow-axis-polarized light acquires a $\pi/2$ phase shift with respect to the orthogonally-polarized component. As a result, the beam field \mathbf{E}_1 after the QWP is described by the following Jones-matrix transformation [S8]:

$$\begin{pmatrix} E_{1,x} \\ E_{1,y} \end{pmatrix} = \begin{pmatrix} \sin^2\phi + i\cos^2\phi & \sin\phi\cos\phi(1-i) \\ \sin\phi\cos\phi(1-i) & i\sin^2\phi + \cos^2\phi \end{pmatrix} \begin{pmatrix} E_{0,x} \\ E_{0,y} \end{pmatrix}. \quad (\text{S9})$$

Substituting here Eq. (S8) and omitting the common $(1-i)/\sqrt{2}$ factor, we obtain

$$\begin{pmatrix} E_{1,x} \\ E_{1,y} \end{pmatrix} = \frac{E_0}{\sqrt{2}} \begin{pmatrix} \sin 2\phi \\ i + \cos 2\phi \end{pmatrix} \exp(ikz). \quad (\text{S10})$$

After the QWP, the beam is redirected by the mirror, which works as an ideal reflector: the sign of the y -component of the field flips (which is equivalent, up to a total phase factor, to the $\phi \rightarrow -\phi$ transformation). Therefore, the field of the beam entering the objective lens becomes

$$\begin{pmatrix} E_{1,x} \\ E_{1,y} \end{pmatrix} = \frac{E_0}{\sqrt{2}} \begin{pmatrix} \sin 2\phi \\ -i - \cos 2\phi \end{pmatrix} \exp(ikz). \quad (\text{S11})$$

Next, the beam enters the glass (a high-NA objective in our case, see Figs. S1 and S6 below) and undergoes a total internal reflection at the glass-air interface. The generation of the evanescent field and its properties at such interface are described in detail in the Supplementary Materials of [7]. Following that work, we represent the field (S11) inside the glass in three-dimensional form:

$$\mathbf{E}_1 \equiv \begin{pmatrix} E_{1,x} \\ E_{1,y} \\ E_{1,z} \end{pmatrix} = \frac{E_0}{\sqrt{1+|m_1|^2}} \begin{pmatrix} 1 \\ m_1 \\ 0 \end{pmatrix} \exp(in_1 kz), \quad (\text{S12})$$

where

$$m_1 = \frac{E_{1,y}}{E_{1,x}} = -\frac{i + \cos 2\phi}{\sin 2\phi} \quad (\text{S13})$$

is the complex polarization parameter, and $n_1 = 1.5$ is the refractive index of the glass.

The plane-wave field (S12) impinges the glass-air interface with the angle of incidence α , $n_1 \sin \alpha > 1$ ($\alpha \approx 54.6^\circ$ in our experiment). The evanescent wave field \mathbf{E} generated in the air can be written as (see Supplementary Materials of [7])

$$\mathbf{E} \equiv \begin{pmatrix} E_x \\ E_y \\ E_z \end{pmatrix} = \frac{E}{\sqrt{1+|m|^2}} \begin{pmatrix} 1 \\ mk/k_z \\ -i\kappa/k_z \end{pmatrix} \exp(ik_z z - \kappa x), \quad (\text{S14})$$

where

$$k_z = kn_1 \sin \alpha \equiv k \cosh \vartheta, \quad \kappa = \sqrt{k_z^2 - k^2} \equiv k \sinh \vartheta, \quad (\text{S15})$$

are the propagation and exponential-decay wavevector parameters of the evanescent wave, which are expressed via the hyperbolic angle ϑ . (In our experiment the propagation wavelength $2\pi k_z^{-1} \approx 532$ nm and decay scale of the evanescent wave $\kappa^{-1} \approx 150$ nm.) In Eq. (S14) we used the (x, y, z) coordinates shown in **Figures 1 and 2**, and introduced the following amplitude and polarization parameters:

$$E = \frac{k}{k_z} \sqrt{\frac{1+|m|^2}{1+|m_1|^2}} T_p E_0, \quad m = \frac{T_s}{T_p} m_1, \quad (\text{S16})$$

which involve the Fresnel transmission coefficients [12]

$$T_s = \frac{2n_1 \cos \alpha}{n_1 \cos \alpha + i \sinh \vartheta}, \quad T_p = \frac{2n_1 \cos \alpha}{\cos \alpha + i n_1 \sinh \vartheta}. \quad (\text{S17})$$

Equations (S13)–(S17) completely describe the evanescent wave electric field $\mathbf{E}(\mathbf{r})$ that we probe in the experiment. Substituting this field into the general equations (S5)–(S7), we obtain the canonical and spin momentum densities in the evanescent wave:

$$\mathbf{P}^{\text{can}} = \frac{W}{\omega} k_z \left(1 + \tau \frac{\kappa^2}{k_z^2} \right) \bar{\mathbf{z}} = \frac{W}{\omega} k \left(\cosh \vartheta + \tau \frac{\sinh^2 \vartheta}{\cosh \vartheta} \right) \bar{\mathbf{z}}, \quad (\text{S18})$$

$$\mathbf{P}^{\text{spin}} = \frac{W}{\omega} \left(-\frac{\kappa^2}{k_z} \bar{\mathbf{z}} + \sigma \frac{\kappa k}{k_z} \bar{\mathbf{y}} \right) = \frac{W}{\omega} k \left(-\frac{\sinh^2 \vartheta}{\cosh \vartheta} \bar{\mathbf{z}} + \sigma \frac{\sinh \vartheta}{\cosh \vartheta} \bar{\mathbf{y}} \right). \quad (\text{S19})$$

We also determine the imaginary Poynting vector:

$$\text{Im } \mathcal{P} = \frac{W}{\omega} \left(-\tau \frac{\kappa k^2}{k_z^2} \bar{\mathbf{x}} - \chi \frac{\kappa k}{k_z} \bar{\mathbf{y}} \right) = \frac{W}{\omega} k \left(-\tau \frac{\sinh \vartheta}{\cosh^2 \vartheta} \bar{\mathbf{x}} - \chi \frac{\sinh \vartheta}{\cosh \vartheta} \bar{\mathbf{y}} \right), \quad (\text{S20})$$

which will play role in calculations of weak transverse optical forces. In equations (S18)–(S20) $W = \frac{1}{4}(|\mathbf{E}|^2 + |\mathbf{B}|^2) = \frac{1}{2}|E|^2 \exp(-2\kappa x)$ is the energy density of the field, $\bar{\mathbf{x}}$, $\bar{\mathbf{y}}$ and $\bar{\mathbf{z}}$ are the unit vectors of the corresponding axes, whereas

$$\tau = \frac{1-|m|^2}{1+|m|^2}, \quad \chi = \frac{2 \text{Re } m}{1+|m|^2}, \quad \sigma = \frac{2 \text{Im } m}{1+|m|^2} \quad (\text{S21})$$

are the Stokes parameters of the evanescent field [7]. In particular, the third Stokes parameter σ is the degree of circular polarization, i.e., *helicity*, which determines the longitudinal z -directed *spin angular momentum* of light.

Substituting Eqs. (S13)–(S17) into Eq. (S21), we express the Stokes parameters of the evanescent wave as functions of the varying QWP angle ϕ and other parameters:

$$\begin{aligned} \tau &= \frac{\sin^2 2\phi - (\cos^2 2\phi + 1)(\cosh^2 \vartheta - \cos^2 \alpha)}{\sin^2 2\phi + (\cos^2 2\phi + 1)(\cosh^2 \vartheta - \cos^2 \alpha)}, \\ \chi &= 2 \frac{\sin 2\phi (-\cos 2\phi \cosh \vartheta \sin \alpha + \sinh \vartheta \cos \alpha)}{\sin^2 2\phi + (\cos^2 2\phi + 1)(\cosh^2 \vartheta - \cos^2 \alpha)}, \\ \sigma &= -2 \frac{\sin 2\phi (\cosh \vartheta \sin \alpha + \sinh \vartheta \cos \alpha \cos 2\phi)}{\sin^2 2\phi + (\cos^2 2\phi + 1)(\cosh^2 \vartheta - \cos^2 \alpha)}. \end{aligned} \quad (\text{S22})$$

Importantly, the parameters $\tau(\phi)$, $\chi(\phi)$, and $\sigma(\phi)$ show different behaviour with variations of the QWP angle ϕ , which enables us to separate the τ -, χ - and σ -dependent effects in our ϕ -dependent measurements. In particular, $\tau(\phi)$ is an *even* function of ϕ , while $\chi(\phi)$ and $\sigma(\phi)$ are *odd* functions. This yields a remarkable result: all *longitudinal* (z -directed) and *vertical* (x -directed) field properties in Eqs. (S18)–(S20) are *even* functions of ϕ , while all *transverse* (y -directed) characteristics are *odd*. This allows an efficient separation of the usual in-plane and extraordinary transverse phenomena in ϕ -dependent measurements. Note that the energy density $W(\phi)$ is also an even function of ϕ :

$$W \propto |E_0|^2 \frac{2 \cot^2 \alpha}{(n_1^2 - 1)} \left(\frac{\sin^2 2\phi}{\cosh^2 \vartheta - \cos^2 \alpha} + \cos^2 2\phi + 1 \right), \quad (\text{S23})$$

which does not affect the above features of the polarization dependences.

It should be noticed that the polarization Stokes parameters in Eqs. (S18)–(S22) are those of the *evanescent* wave, and are determined via its polarization parameter m . This polarization and Stokes parameters are slightly different from those of the *incident beam*; the latter are described by Eqs. (S21) with the polarization parameter m_1 . We use both kinds of Stokes parameters in this paper, to conveniently characterize the polarization at different stages. For instance, the polarization of the *incident* wave is depicted on the Poincaré sphere in Fig. 2c and indicated schematically under the ϕ -axes in Figs. 3 and S2–S4. At the same time, discussing the τ -, χ -, and σ -contributions to optical momenta and forces, we imply the Stokes parameters of the evanescent wave.

Equations (S18)–(S20) show the presence of different kinds of optical momenta in the evanescent wave. The first one is the longitudinal τ -dependent canonical momentum density P_z^{can} , proportional to the wavevector component k_z [shown in the cyan frames in (S18)]. As $k_z > k = \omega/c$, this momentum density exceeds $\hbar\omega/c$ per photon. Therefore, the canonical momentum in an evanescent wave produces anomalously-high radiation pressure, which has been experimentally measured using light-atom interactions [22,14]. Second, the evanescent wave exhibits the spin momentum, which has a σ -dependent component P_y^{spin} , *perpendicular to both the propagation and decay directions of the wave* [shown in the magenta frames in (S19)]. This helicity-dependent transverse momentum is the main subject of our work. Finally, Eq. (S20) shows that the imaginary Poynting vector also has a transverse y -directed component $\text{Im} \mathcal{P}_y$

[shown in the light magenta frames], which is proportional to the second Stokes parameter χ . As we show below (Section 2), this component also contributes to the weak transverse force on matter probes [7].

Note that the longitudinal component of the spin momentum in Eq. (S19), P_z^{spin} , produces only a weak τ -dependent (i.e., ϕ -even) correction to the strong radiation-pressure force from the canonical momentum, and, hence, can be ignored. Furthermore, its magnitude has a smallness of $\propto \kappa^2$ when $\kappa \ll k$. This longitudinal spin momentum is associated with another intriguing phenomenon: the transverse helicity-independent spin in evanescent waves [7,27,S5,S9–S13]. Similarly, the vertical component of the imaginary Poynting vector in Eq. (S20), \mathcal{P}_x , produces only a weak τ -dependent correction to the strong vertical gradient force.

2. Calculations of optical forces and comparison with the experiment

Having the evanescent field (S13)–(S17) and its momentum properties (S18)–(S23), we now calculate how these properties reveal themselves in interactions with matter probes immersed in the evanescent wave. The momentum transfer in light-matter interactions produces optical forces, which we calculate below.

2.1. Calculations of the forces using the spherical-particle model

We first consider the simplest analytical model of a small spherical isotropic dielectric particle of radius $r \ll \lambda$ and permittivity ε [7,8]. In the lowest orders in $kr \ll 1$, such a particle is characterized by the complex electric polarizability v_e :

$$\text{Re}v_e = r^3 \frac{\varepsilon - 1}{\varepsilon + 2}, \quad \text{Im}v_e = \frac{2}{3}k^3 (\text{Re}v_e)^2, \quad (\text{S24})$$

where the small imaginary part, $|\text{Im}v_e| \ll |\text{Re}v_e|$, originates from the radiation-friction effects [24,S14,S15]. The lowest-order magnetic polarizability of the particle is [S14]

$$v_m = k^2 r^5 \frac{\varepsilon - 1}{30}, \quad (\text{S25})$$

so that $|\text{Re}v_m| \ll |\text{Re}v_e|$ and $\text{Im}v_m \approx 0$.

In the leading-order electric-dipole approximation, the optical force is given by [7,8,21,S4,S6,S15,S16]:

$$\mathbf{F} \propto \text{Re}(v_e) \nabla W_e + \frac{1}{2} \omega \text{Im}(v_e) \mathbf{P}^{\text{can}}. \quad (\text{S26})$$

Here the first term is the *gradient* force \mathbf{F}^{grad} involving the electric energy density $W_e = |\mathbf{E}|^2 / 4$, and the second term is the *radiation pressure* force $\mathbf{F}^{\text{press}}$ proportional to the *canonical momentum density* \mathbf{P}^{can} . In the evanescent wave under consideration, the gradient force is directed along the vertical x -axis of the exponential decay, i.e., along the normal to the interface, while the radiation pressure is associated with the longitudinal z -direction of propagation and the canonical momentum density (S18).

Calculating the next-order correction to the electric-dipole force (S26), one can obtain a weak force, which originates from the dipole-dipole interaction between the electric and magnetic polarizabilities of the particle [7,8,24,S6]:

$$\delta \mathbf{F} \propto -\frac{\omega k^3}{3} \left[\text{Re}(v_e v_m^*) \mathbf{P}^{\text{can}} + \underbrace{\text{Re}(v_e v_m^*) \mathbf{P}^{\text{spin}}}_{\mathbf{F}^{\text{spin}}} + \underbrace{\text{Im}(v_e v_m^*) \text{Im} \mathcal{P}}_{\mathbf{F}^{\text{lm}}} \right]. \quad (\text{S27})$$

The first term, proportional to \mathbf{P}^{can} , is only a small correction to the radiation-pressure force in Eq. (S26), and it can be ignored in our considerations. The second term, proportional to \mathbf{P}^{spin} , is the *weak spin force* \mathbf{F}^{spin} associated with the *Belinfante spin momentum*. It is mostly *transverse*, i.e., y -directed in the evanescent wave with $\kappa \ll k_z$. Note that for dielectric particles $\text{Re}(v_e v_m^*) > 0$, and this force is *negative*, i.e., antiparallel to the spin-momentum direction. For non-absorbing dielectric particles, $k^3 |\text{Re}(v_e v_m^*)| \propto k^5 r^8$ and $|\text{Im}v_e| \propto k^3 r^6$, so that $|\mathbf{F}^{\text{spin}}| / |\mathbf{F}^{\text{press}}| \propto (kr)^2 \ll 1$. Finally, the third term in (S27) is proportional to the *imaginary*

Poynting vector $\text{Im } \mathcal{P}$, and it also has the transverse y -directed component. For small particles with $kr \ll 1$, this force is much weaker than the spin-momentum force, $|\mathbf{F}^{\text{lm}}| \ll |\mathbf{F}^{\text{spin}}|$, because $k^3 |\text{Im}(\mathbf{v}_e \mathbf{v}_m^*)| \propto k^8 r^{11}$. However for larger objects with $kr \sim 1$ (which is the case in our experiment), the force \mathbf{F}^{lm} also becomes noticeable.

In this work, we measure: (i) the longitudinal radiation-pressure force $F_z = F_z^{\text{press}} \propto P_z^{\text{can}}$ and (ii) the weak transverse force F_y , which includes the spin force $F_y^{\text{spin}} \propto P_y^{\text{spin}}$ and the imaginary-Poynting contribution $F_y^{\text{lm}} \propto \text{Im } \mathcal{P}_y$. Importantly, using the polarization dependences of these forces in the evanescent wave, Eqs. (S18)–(S23), we can clearly separate the above contributions even if they are mixed by a complex-shape probe (such as a cantilever). Namely, all the longitudinal (and also vertical) forces in Eqs. (S26) and (S27) depend only on the *first Stokes parameter* τ , and therefore are *even* functions of the QWP angle ϕ . In turn, the transverse spin force and transverse imaginary-Poynting contribution are proportional to the *third Stokes parameter* σ (helicity) and the *second Stokes parameter* χ , respectively. Therefore, both these parts of the transverse force are *odd* functions of the QWP angle ϕ . Thus, the ϕ -even and ϕ -odd parts of the total force $F(\phi)$ measured by the cantilever, $F^{\text{even}}(\phi) \equiv [F(\phi) + F(-\phi)]/2$ and $F^{\text{odd}}(\phi) \equiv [F(\phi) - F(-\phi)]/2$, correspond to the longitudinal and transverse forces in the particle model.

In spite of its highly simplified character, the spherical-particle model can be used to characterize optical forces measured by the complex-shape cantilever in our experiment. Here we have to deal with not-small particles $kr \sim 1$ (because the cantilever thickness d is not small: $kd \sim 1$). Therefore we use exact Mie-particle calculations [7], which take into account higher-order corrections to the electric and magnetic polarizabilities (S24) and (S25) but do not affect the general proportionality to the field momenta and the corresponding polarization parameters, Eqs. (S26) and (S27). The dielectric constant of the particle is set as that of the cantilever: $\varepsilon = n^2 = 5.3$. To compare the particle model and cantilever measurements, we involve three fitting parameters. First, the radius of the particle, r , is the main free parameter of the model. It controls the ratio between the σ -dependent and χ -dependent contributions in the transverse force F_y . Second, since the weighting factors of the longitudinal and transverse forces mixed in the cantilever measurements depend on the shape effects, and also the total wave intensity is unknown, we introduce the scaling coefficients $K_{\parallel, \perp}$ between the calculated and measured quantities. As we are interested in the ϕ -dependences of the forces, we consider the difference between the maximum and minimum values of the longitudinal radiation-pressure force $F_z^{\text{press}}(\phi)$:

$$\left\{ \max [F^{\text{even}}(\phi)] - F(0) \right\}_{\text{measured}} = K_{\parallel} \left\{ \max [F_z^{\text{press}}(\phi)] - F_z^{\text{press}}(0) \right\}_{\text{calculated}}, \quad (\text{S28})$$

$$\left\{ F^{\text{odd}}(\phi) \right\}_{\text{measured}} = K_{\perp} \left\{ F_y(\phi) \right\}_{\text{calculated}}. \quad (\text{S29})$$

The results of the comparison between the particle-model calculations and experimentally-measured forces are shown in Fig. S2. Using the scaling relation (S28), the calculated longitudinal radiation-pressure force (S26), $F_z^{\text{press}}(\phi) - F_z^{\text{press}}(0)$, is in very good agreement with the measured one, independently of the particle radius r . This is because the ϕ -dependence of this force is determined by the first Stokes parameter $\tau(\phi)$, independently of r . At the same time, the ϕ -dependence of the calculated transverse force (S27), $F_y(\phi)$, depends on the radius and shows the best agreement with the experiment for $r \approx 139$ nm (i.e., comparable with the

cantilever thickness $d \approx 100$ nm). This corresponds to the value $kr \approx 1.32$, for which both the spin contribution F_y^{spin} , proportional to $\sigma(\phi)$, and the imaginary-Poynting contribution F_y^{Im} , proportional to $\chi(\phi)$, play a role. The perfect agreement between the polarization ϕ -dependences of the experimentally-measured and calculated forces proves that the measured even and odd parts of the total cantilever force can indeed be associated with the longitudinal and transverse optical forces. In turn, these forces are determined by the canonical momentum P_z^{can} and transverse Belinfante momentum P_y^{spin} , together with the imaginary Poynting momentum $\text{Im}\mathcal{P}_y$, in the evanescent wave. Such robust polarization dependences of different forces, independently of the probe shape, confirm that we deal with intrinsic field properties. This is in contrast to “extrinsic” spin-dependent transverse-force effects, which originate from the probe-interface interactions [28–30] or specific properties of the probe, such as chirality [S4,S17–S19]. Note that in the case of chiral probes even the usual dipole radiation-pressure and gradient forces become spin- and helicity-dependent [S4,S17,S20–S22].

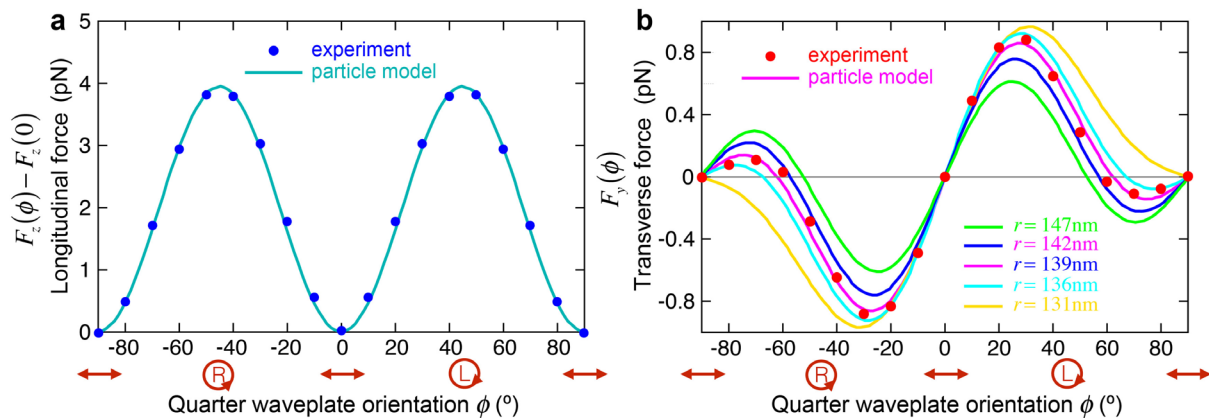


Figure S2. Longitudinal (a) and transverse (b) optical forces in an evanescent wave, calculated for a spherical particle, Eqs. (S26) and (S27), and fitted to the even and odd parts of the experimentally-measured force on the cantilever. The fitting procedure includes the scaling (S28) and (S29) and the fitting of the particle radius.

It is worth noticing that in the isotropic spherical-particle model, the longitudinal radiation-pressure force has the same order of magnitude for the p - and s -polarizations of light ($\tau = 1$ and $\tau = -1$). In contrast, for a cantilever with a highly-anisotropic vertical shape, the radiation-pressure force becomes very small for the horizontally s -polarized light. This difference between the particle and cantilever probes is not seen in our plots because we scale the variations of the radiation-pressure with respect to the s -polarized light ($\phi = 0$), Eq. (S28).

2.2. Numerical calculations of the forces for the cantilever

For numerical simulations of the interaction between the evanescent optical field and the cantilever, we employ the Coupled Dipole Method (CDM) [S23,S24]. In this method, continuous matter objects are decomposed into cubic arrays of point polarizable dipoles (cells) coupled through the electromagnetic dipole interaction tensor. When exposed to an external field, each cell feels not only the incident field but also the field scattered by all the other cells in the structure. Algebraically, this results in a large set of linear equations whose solution yields the polarization of each cell. Our implementation of this method for the simulation of the mechanical

action of light is discussed elsewhere [S25], and we use the Quasi-Minimal Residual Method (QMR) [S26] with matrix-vector multiplication accelerated by fast Fourier transforms [S27].

The total (incident plus scattered) field outside the matter object is then given by the sum of the incident field with all of the radiating dipole fields. As the numerical lattice is refined, the total field converges to the continuum result. This approach lends itself well to structures of extreme geometry, such as the cantilever used in our experiment. Once the total field is known, the time-averaged optical force acting on each cell can be found by calculating the flux of the Maxwell stress tensor [S14,S24,S25,S28,S29].

In our simulations, the incident evanescent field is given by Eqs. (S13)–(S17) with the corresponding parameters of the experiment, while the cantilever is modelled as a dielectric cuboid with permittivity $\varepsilon = n^2 = 5.3$. If not otherwise stated, we use the following geometric parameters of the cantilever: thickness $d = 140$ nm (obtained from the fitting procedure described below), width $w = 1000$ nm, and infinite vertical length $l \rightarrow \infty$. Convergence of the model has been achieved by (i) refining the numerical lattice, (ii) increasing the vertical length l of the cantilever. The resulting model uses $N \sim 2.5 \cdot 10^6$ cells and $l = 500$ nm (this value approximately equals to the triple decay length $3\kappa^{-1} \simeq 450$ nm, and further increase of l practically does not affect the simulation results).

To characterize the $y \rightarrow -y$ asymmetry of the real cantilever (Figs. 2b,d), which couples the longitudinal radiation pressure to the transverse direction, we rotate the ideal symmetric (cuboidal) cantilever in numerical simulations by a small angle $\theta \simeq 0.08$ (i.e., 4.7°) with respect to the z -axis in the (y,z) -plane, as shown in Fig. S3a. We numerically calculate the force $\mathbf{F}^{\text{numeric}}(\phi) = F^{\text{numeric}}(\phi)\bar{\mathbf{n}}$ directed along the normal $\bar{\mathbf{n}}$ to the cantilever surface, which mixes the weak transverse force $F_y(\phi)$ and the radiation pressure $F_z^{\text{press}}(\phi)$ contributions. Using two fitting parameters: (i) the cantilever thickness d and (ii) its orientation angle θ , we fit the numerically-calculated force $F^{\text{numeric}}(\phi)$ to the measured force $F^{\text{measured}}(\phi)$ using only the common scaling factor (as the light intensity is unknown). With the values $\theta \simeq 0.08$ and $d = 140$ nm we achieve perfect agreement between the numerical simulations and experimental measurements, as shown in Fig. S3b.

Next, we decompose the total calculated force $F^{\text{numeric}}(\phi)$ into three contributions, proportional to the polarization Stokes parameters τ , χ , and σ (the small polarization-independent contribution is ignored). First, the τ -dependent contribution is associated with the radiation-pressure force F^{press} (S26) proportional to the τ -dependent canonical-momentum P_z^{can} (S18). This force is an even function of the QWP angle ϕ , and it is shown in Fig. S3c. Second, the χ - and σ -dependent contributions constitute the weak transverse force (S27) [7]; their odd ϕ -dependences are shown in Fig. S3d. The helicity-dependent σ -contribution is associated with the transverse Belinfante spin momentum in the evanescent wave: $F_y^{\text{spin}} \propto P_y^{\text{spin}}$ (Fig. 1). At the same time, the χ -dependent part is the transverse force associated with the imaginary Poynting vector: $F_y^{\text{Im}} \propto \text{Im} \mathcal{P}_y$. It is also clearly present, both in simulations and measurements because the cantilever thickness is not small: $kd \sim 1$. The presence of the χ -dependent contribution to the transverse force allows to discriminate between the “intrinsic” transverse force predicted in [7,8], which originates from the inherent field properties, and “extrinsic” spin-dependent transverse forces which arise from the coupling between the probe and an interface [28–30].

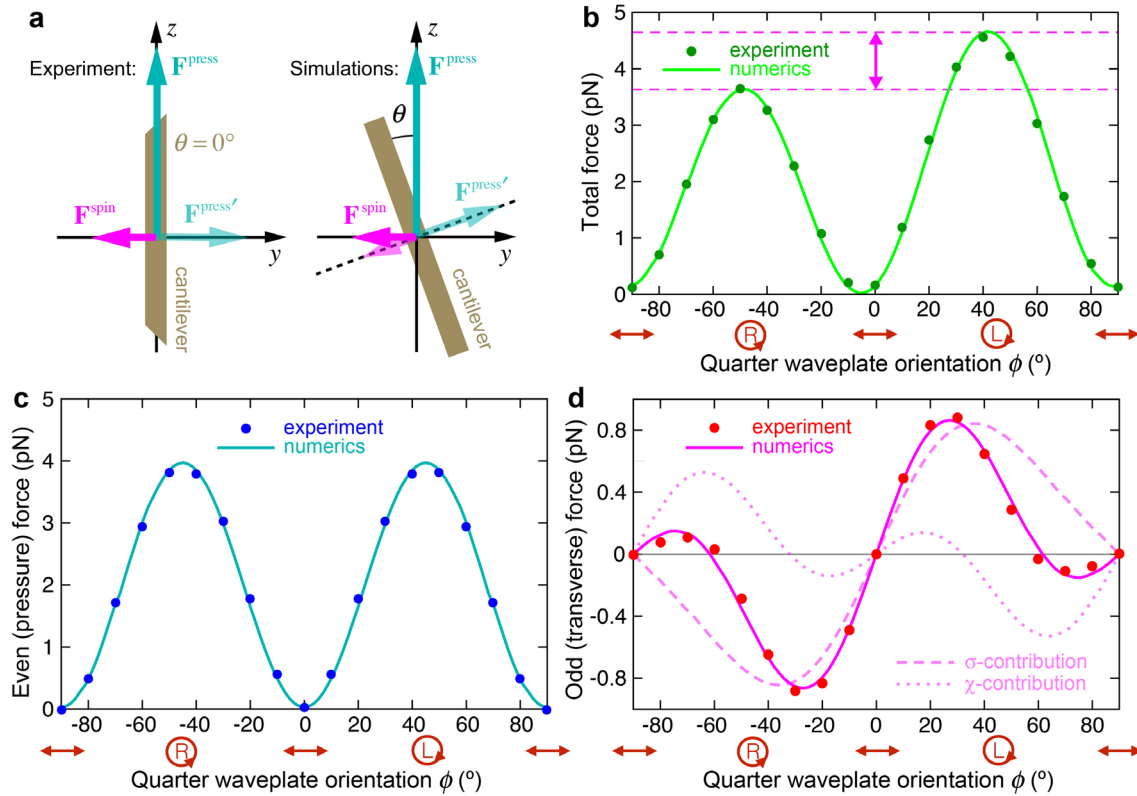


Figure S3. (a) Schematics of the mixing of the longitudinal radiation pressure with the transverse force in the field interaction with an $y \rightarrow -y$ asymmetric cantilever. Left: an asymmetric cantilever used in the experiment (see Fig. 2b). Right: symmetric but slightly rotated cantilever used in numerical simulations. (b) The total force $F(\phi)$ acting in the normal direction to the cantilever. Numerical simulations perfectly match the experimental measurement using the two fitting parameters: the cantilever thickness d and its orientation angle θ . (c,d) The ϕ -even (c) and ϕ -odd (d) parts of the total force $F(\phi)$ are associated with the longitudinal radiation pressure and weak transverse force, as shown in Fig. S2. The σ -dependent and χ -dependent contributions to the transverse force, associated with the Belinfante spin momentum and imaginary Poynting vector are separately shown in (d).

To verify that the τ -dependent force in the experiment is indeed caused by the $y \rightarrow -y$ asymmetry of the cantilever, we note that it vanishes in numerical simulations with a perfectly-aligned symmetric cantilever: $\theta = 0$. To check the correspondence between the model asymmetry parameter θ and the $y \rightarrow -y$ asymmetry of the real cantilever, we also performed measurements with the same cantilever rotated by 180° about its vertical x -axis, which corresponds to the $y \rightarrow -y$ and $z \rightarrow -z$ transformations. Simultaneously, we changed the sign of θ in the numerical simulations, see Fig. S4a. The results, shown in Fig. S4, clearly demonstrate that the above transformations flip the even (radiation-pressure) part of the force, while leaving the odd (transverse) part of the force essentially unchanged. Some imperfections of these transformations between Fig. S3 and Fig. S4 are explained by the fact that these correspond to two independent experiments with re-assembling of the setup and also by the $z \rightarrow -z$ asymmetry of the real cantilever (Fig. 2b). These factors are taken into account by a new fitting procedure, which resulted in the value $\theta \approx -0.1$ (i.e., -5.6°) for the “flipped” experiment in Fig. S4.

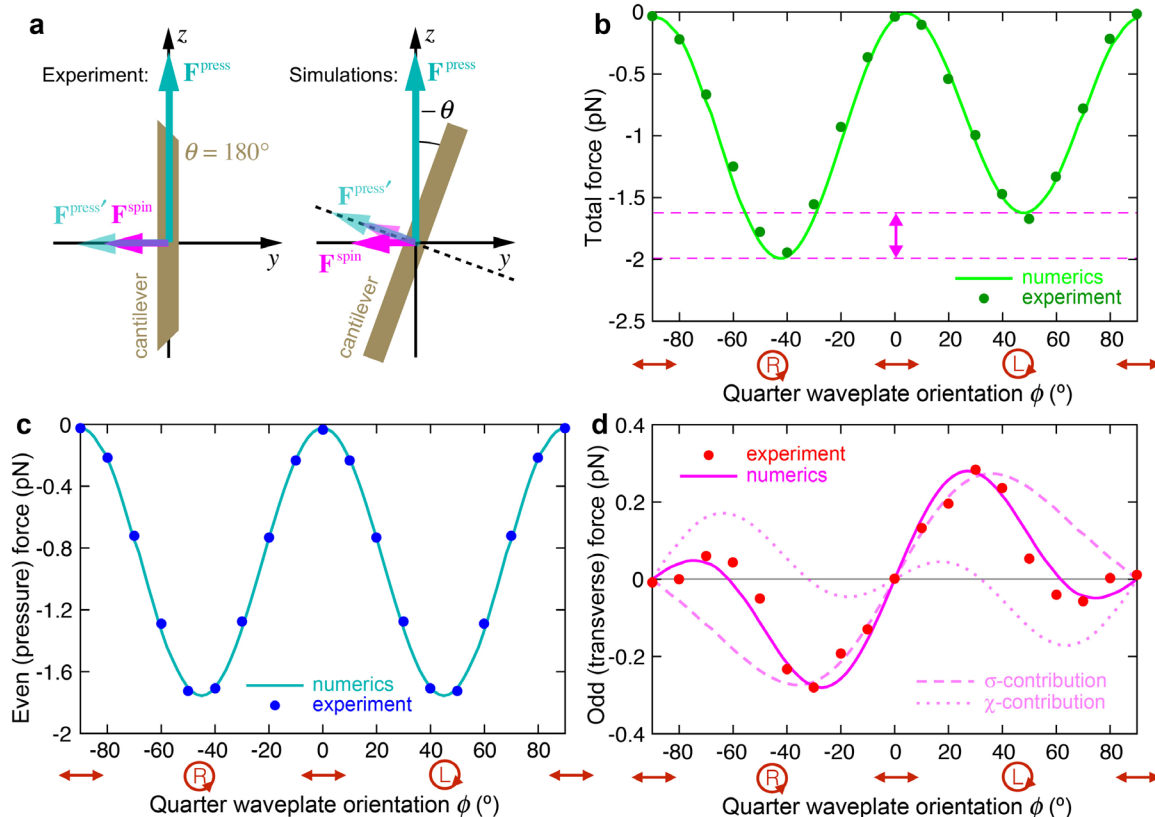


Figure S4. Same as in Fig. S3 but for the “flipped” cantilever: rotated by 180° about the x -axis in the experiment and oriented at the negative angle $-\theta$ in numerical simulations (cf. Fig. S3a and Fig. S4a). The flip of the ϕ -even (radiation-pressure) part of the force proves that it is caused by the $y \rightarrow -y$ asymmetry of the cantilever. At the same time the ϕ -odd (transverse) force remains almost unchanged, which proves that this is a robust field phenomenon.

Finally, using numerical simulations, we also investigated the dependences of the longitudinal and transverse forces on the *area* of the cantilever. This was done by calculating the forces at fixed QWP angle ϕ and varying the cantilever width w . To save simulation time, we modelled a thin cantilever with $d = 50$ nm, for which the imaginary-Poynting contribution to the transverse force is negligible. The results are shown in Fig. S5. One can see that the ϕ -even force associated with the longitudinal radiation pressure grows near-linearly with w , which reflects its usual radiation-pressure nature related to the *planar surface* of the cantilever. In contrast to this, the ϕ -odd force, associated with the transverse Belinfante spin momentum, approximately *saturates* after w reaches few wavelengths. This means that the helicity-dependent force associated with the Belinfante spin momentum is *not a pressure force, but rather an edge effect related to wave diffraction on the vertical edges of the cantilever*. Indeed, one can show analytically that the transverse force *vanishes* for an infinite lamina without edges aligned with the (x, z) -plane: $F_y^{\text{spin}} = 0$. This is in extreme contrast to the *infinite* radiation-pressure force for the same lamina in the (y, z) -plane: $F_z^{\text{press}} = \infty$. In other words, this proves that the Belinfante spin momentum is indeed “virtual”, and it does not exert the usual radiation pressure on planar objects. Nonetheless, it can be detected (as we do this in the present work) due to its weak interaction with the edges of finite-size probes.

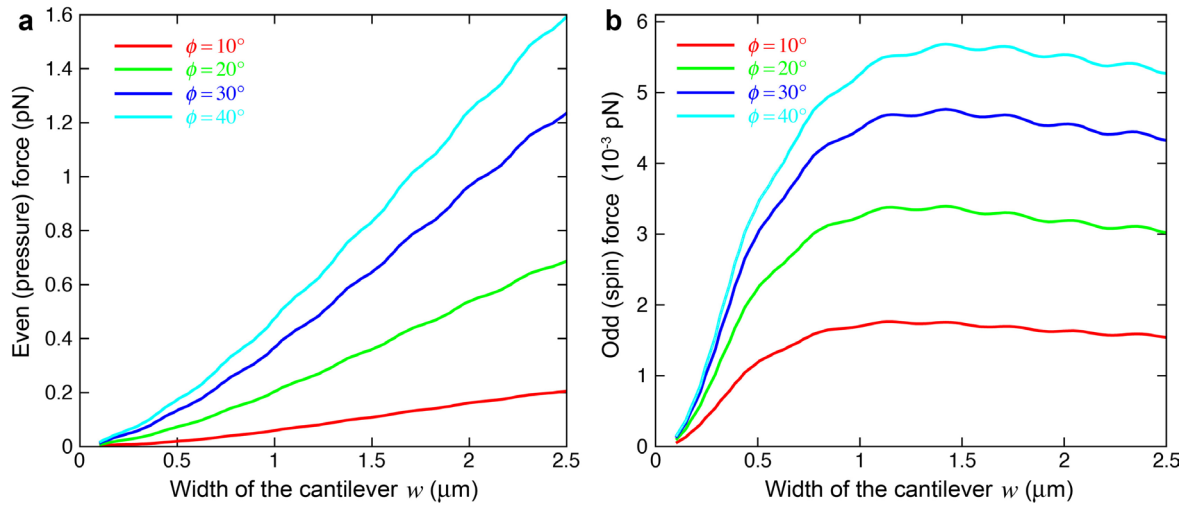


Figure S5. Numerically-calculated ϕ -even (**a**) and ϕ -odd (**b**) parts of the total force acting on the cantilever versus the cantilever width w . The linear growth of the even force reveals its radiation-pressure nature (proportional to the *area* of the cantilever surface). In contrast, the saturation of the odd (transverse) spin-dependent force indicates that it is produced by the field diffraction on the vertical *edges* of the cantilever.

3. Experimental measurements of optical forces using a nano-cantilever

Here we describe details of the experimental setup and measurements. In addition to the force measurements described in the main text and in Section 2 above, we performed a number of extra measurements of the field and cantilever properties in order to determine their parameters and control the system.

3.1. Characterization of the laser field

The experimental setup is shown in **Figure 2a**. Two laser beams, orthogonal to each other, undergo a total internal reflection in a high numerical aperture (NA) objective lens and produce concentric evanescent areas above the glass cover slip of the objective (**Fig. S6**). The red laser 1 (Cube from Coherent Inc.) operates with a wavelength $\lambda = 660$ nm and power 50 mW. This radiation, with the polarization controlled using the QWP, is the source of the evanescent field under consideration. The green laser 2 (Versa-lase from Vortran Laser Technology Inc.) has a wavelength $\lambda' = 561$ nm and power 50 mW; its radiation is p -polarized at the glass-air interface where the evanescent field is formed. This radiation is used for measuring the cantilever position.

The evolution of the laser beams in the high-NA objective and generation of the evanescent wave is illustrated in **Figure S6** (the laser-1 beam is shown). The input off-axis laser beam is focused in the back focal plane of the high-NA objective lens. The off-axis refraction at the objective lens forms a collimated beam propagating at the refraction angle α , which depends on the displacement of the incident beam. At a certain off-axis distance, the condition for total internal reflection at the cover-slip surface is reached (for refractive index $n_1 = 1.5$, the critical angle of incidence is $\alpha_c = 41.8^\circ$), and the evanescent field is generated in the air above the surface.

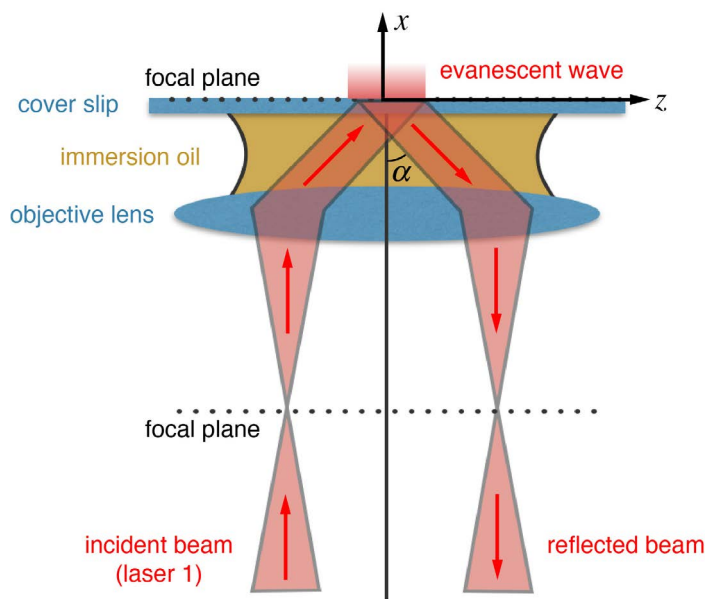


Figure S6. Formation of the evanescent field by the total internal reflection of the off-axis laser-1 beam in the high-NA objective covered by a glass slip. The laser-2 beam forms a similar concentric evanescent field in the orthogonal (x,y) -plane.

In this technique, we cannot measure the angle of incidence α directly, but it can be determined from the exponential decay length κ^{-1} of the evanescent wave (i.e., the x -distance above the glass surface where the field amplitude drops by a factor of e^{-1}). We determined the decay length by measuring the displacement of the cantilever by the p -polarized laser 1 (which is proportional to the scattered intensity of the laser-1 radiation) as the cantilever tip is moved away from the surface, Fig. S7. Fitting the data with an exponential function results in a decay length $\kappa^{-1} = (150 \pm 4)$ nm. According to Eqs. (S14) and (S15), this corresponds to the angle of incidence $\alpha = 54.6^\circ \pm 0.5^\circ$.

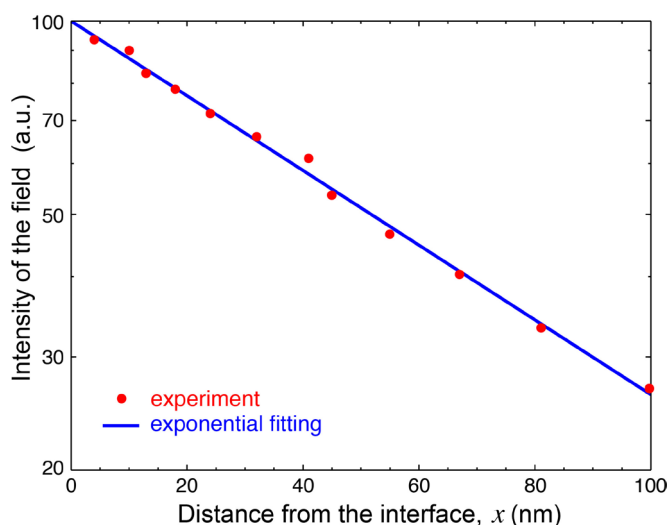


Figure S7. Measurement of the exponential decay of the evanescent-wave intensity (laser 1 here) above the glass surface.

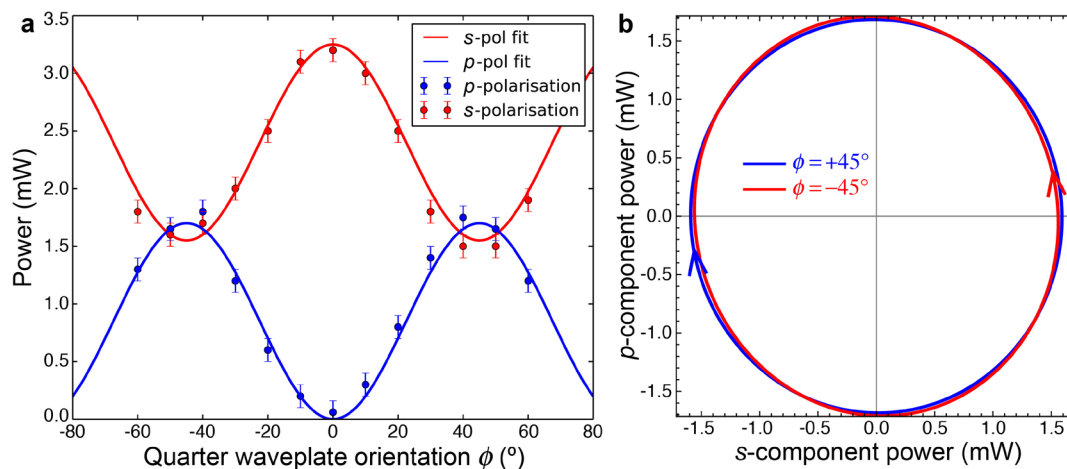


Figure S8. (a) The measured s and p components of the incident-beam polarization after the QWP and mirror. (b) Right-hand and left-hand circular polarizations are obtained for the QWP angles $\phi = \pm 45^\circ$.

The polarization state of the laser-1 field is controlled by the rotating quarter waveplate (QWP) (Figs. 2a and S1). Its orientation is varied in the range of angles $-90^\circ \leq \phi \leq 90^\circ$. Here $\phi = 0^\circ$ corresponds to the linear s -polarization of the beam. Figure S8 shows the measured polarizations of the beam after passing the QWP and mirror, just before entering the objective

lens. In particular, for $\phi = \pm 45^\circ$ the polarization becomes circular with good accuracy [$m_1 = \mp i$ in Eq. (S13)]. The corresponding polarizations in the evanescent wave are slightly elliptical, which is taken into account in Eqs. (S16)–(S22).

3.2. Optical detection of the cantilever position

The cantilever, interacting with the evanescent laser-1 and laser-2 fields, is placed 30 nm above the cover-slip surface (Fig. 2a). It is perpendicular to the surface with an accuracy of 1° and is adjusted to be in the centre of the Gaussian-like area of the evanescent fields (diameter $\sim 50\mu\text{m}$) within $\pm 2\mu\text{m}$. The cantilever deflection is measured using the scattered evanescent wave (SEW) detection system [20] involving the laser-2 radiation. Note that the laser-2 field does not interfere with the laser-1 radiation and does not affect the cantilever interaction with the probed laser-1 field. Furthermore, the reflected laser-2 beam is the only signal reaching the quadrant photodetector, because two sets of filters are used to stop the reflected laser-1 beam (Fig. 2a). We have checked that the cross-talk between the two lasers at the detector is smaller than 0.1%.

We monitor the distance between the cantilever tip and the cover-slip surface using the total intensity of the scattered laser-2 light (the SUM signal produced by the photodetector). This distance is kept constant during the measurements by using a negative feedback loop. We adjust the bending direction of the cantilever (i.e., normal to its plane) to be perpendicular to the propagation (x, z) plane of the laser-1 beam: $\theta = 0$ (Fig. 2d). However, the asymmetric shape of the cantilever (Fig. 2b) introduces the $y \rightarrow -y$ asymmetry to the system, which results in a nonzero radiation-pressure force in the transverse y direction.

3.3. Characterization of the nano-cantilever

The optical forces investigated in this work were detected using different types of cantilevers developed in collaboration with NuNano ltd. The cantilevers were produced from extra low-stress Si_3N_4 film on a Si substrate. The thickness of the film determined the thickness of the cantilever and varied from 50 nm to 200 nm. The length of the cantilevers was adjusted to obtain similar stiffness $\sim 10^{-5}$ N/m. The width of the cantilever was kept constant, $w = 1000$ nm. The force magnitude is determined from the cantilever deflection once the stiffness of the cantilever is known. We determined the stiffness (spring constant) of the cantilever using the following two methods.

(i) We measured the thermal power spectral density (PSD) of the cantilever, $S(f)$ (where f is the frequency), see Fig. S9 for an example of one such measurement. The measured PSD was fitted using the equation for the over-damped harmonic oscillator [S30]:

$$S(f) = \frac{k_B T}{b \pi^2 (f_c^2 + f^2)}, \quad (\text{S30})$$

where k_B is the Boltzmann constant, T is the absolute temperature, $f_c = \gamma / (2\pi b)$ is the corner frequency of the PSD, and b is the damping term. The resulting spring constant for the case shown in Fig. S9 is $\gamma = (2.1 \pm 0.2) \cdot 10^{-5}$ N/m.

(ii) By using the method based on the equipartition theorem [S31], the spring constant can be obtained once the mean square displacement $\langle x^2 \rangle$ of the thermally activated cantilever is

measured. In this case, the spring constant is $\gamma = k_B T / \langle x^2 \rangle$. For the cantilever used in Fig. S9, this yields the spring constant $\gamma = (1.8 \pm 0.2) \cdot 10^{-5}$ N/m.

Thus, the two methods provide very similar results, so that we are confident that the spring constant can be determined within 15% of its actual value.

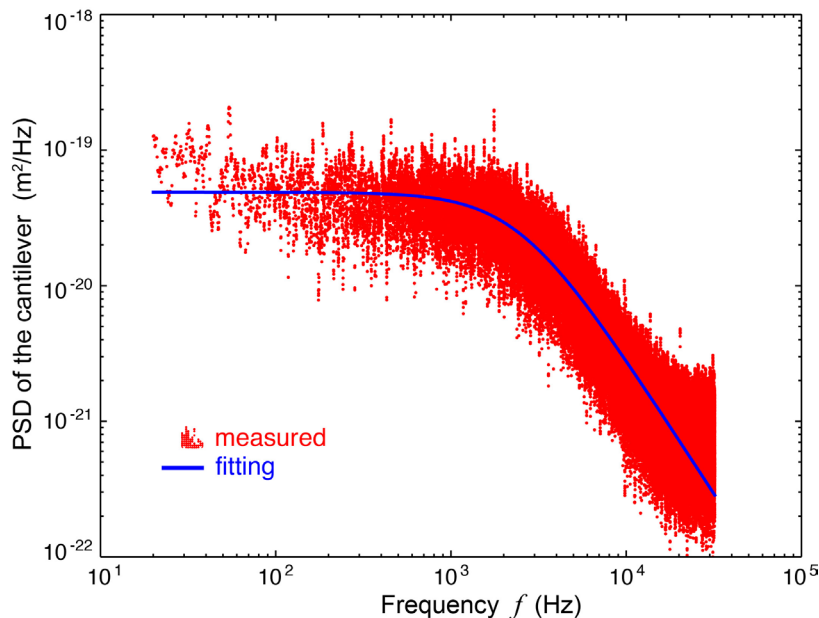


Figure S9. Experimentally-measured PSD of the thermally driven cantilever and its fitting curve obtained using the over-damped harmonic oscillator model (S30).

3.4. Optical force measurements

Knowing the evanescent field properties, as well as the position and the stiffness of the cantilever, we can measure the desired optical forces from the cantilever deflections caused by the laser-1 field.

The intensity of the laser-1 beam is “on-off” modulated in time (TTL modulation) with a frequency of 1 Hz (see Fig. 3a). The deflection of the cantilever, Δ , as well as the modulation signal are recorded at different QWP angles ϕ , from -90° to $+90^\circ$ in steps of 10° . Thus, one complete set of measurements consists of 19 points, each measuring the position of the cantilever for 30 s. We did not notice any significant drift in the instrument during the 15 min necessary to complete a set of measurements.

The data are collected at 64 KHz but decimated by a factor of 100 to remove any cross correlation in the measurements. For each angle of the QWP orientation, the recorded trace is split into two sets of positions: one measured when the laser is “on” and the other one measured when the laser is “off”. Two distributions of positions are generated with their relative mean and the standard error of the mean, as shown in Fig. 3a. The difference of the two mean values is the total displacement $\Delta(\phi)$ caused by the evanescent wave from laser 1. The deflection is finally multiplied by the spring constant to obtain the optical force normal to the cantilever plane: $F(\phi) = \gamma \Delta(\phi)$. To analyse the effects caused by the $y \rightarrow -y$ asymmetry of the cantilever, the measurements were repeated with the cantilever rotated by 180° , as shown in Figs. S3 and S4. To remove inessential force contributions, which do not vary with the QWP orientation (e.g., the gradient force emerging because the cantilever position is not exactly in the centre of the

evanescent area, the possible mechanical action of the laser-2 radiation, etc.), the final data are offset to zero when the beam is *s*-polarized, i.e., when $\phi = 0$.

The results of the measurements of the optical force $F(\phi)$ are depicted in Fig. 3b. Most importantly, the dependence $F(\phi)$ is not symmetric with respect to $\phi \rightarrow -\phi$. This allows us to separate the ϕ -even and ϕ -odd components of the total force, which correspond to the longitudinal radiation-pressure effects and transverse forces. The measurement data for the retrieved forces are shown in Figs. 3c,d and S3, S4.

Thus, in our experiment and calculations, we have carefully traced and verified at all stages the appearance of the longitudinal and transverse optical forces. This allows us to unambiguously associate these measured forces with the longitudinal canonical momentum P_z^{can} , Eqs. (S6) and (S18), transverse Belinfante spin momentum P_y^{spin} , Eqs. (S7) and (S19), and the transverse imaginary Poynting momentum $\text{Im} \mathcal{P}_y$, Eq. (S20), in the evanescent wave [7].

3.5. Additional controls

We note that the above measurements required an extremely low-noise environment without air currents around the probe. Therefore, air conditioning was switched off and a double enclosure was constructed around the LMFM unit.

We also checked that the thermally-induced deflection due to asymmetric illumination of the cantilever was negligible. The measurement protocol described above was repeated with the cantilever rotated by 180° , and it provided the same results within the experimental accuracy. These results confirm earlier findings [S32,S33] that the optical pressure on the cantilever is predominant over the photothermal effect.

Finally, we estimated the longitudinal torque T_z on the cantilever produced by the spin angular momentum S_z of the elliptically-polarized evanescent wave [7]. In principle, such torques could also cause a deflection proportional to the helicity of light. The ratio between the displacements due to the linear force F_y^{spin} and the torque T_z can be estimated as [S34]

$$\frac{(\Delta)_{F_y}}{(\Delta)_{T_z}} = \frac{2F_y^{\text{spin}}}{3T_z} l, \quad (\text{S31})$$

where l is the vertical length of the cantilever. A very conservative approximation, where P_y^{spin} and S_z are used in place of F_y^{spin} and T_z , yields the ratio (S31) of ~ 350 , confirming the negligible effect of the torque.

Supplementary references

- S1. O'Neil, A.T., MacVicar, I., Allen, L. & Padgett, M.J. Intrinsic and extrinsic nature of the orbital angular momentum of a light beam. *Phys. Rev. Lett.* **88**, 053601 (2002).
- S2. Garcés-Chavéz, V., McGloin, D., Padgett, M.J., Dultz, W., Schmitzer, H. & Dholakia, K. Observation of the transfer of the local angular momentum density of a multiringed light beam to an optically trapped particle. *Phys. Rev. Lett.* **91**, 093602 (2003).
- S3. Bliokh, K.Y., Dressel, J. & Nori, F. Conservation of the spin and orbital angular momenta in electromagnetism. *New J. Phys.* **16**, 093037 (2014).
- S4. Bliokh, K.Y., Kivshar, Y.S. & Nori, F. Magnetoelectric effects in local light-matter interactions. *Phys. Rev. Lett.* **113**, 033601 (2014).
- S5. Bliokh, K.Y. & Nori, F. Transverse and longitudinal angular momenta of light. *Phys. Rep.* **592**, 1–38 (2015).
- S6. Ruffner, D.B., Yevick, A. & Grier, D.G. Motion induced by light: photokinetic effects in the Rayleigh limit. arXiv:1505.03806.
- S7. Cameron, R.P. & Barnett, S.M. Electric-magnetic symmetry and Noether's theorem. *New J. Phys.* **14**, 123019 (2012).
- S8. Gerrard, A. & Burch, J.M. *Introduction to matrix methods in optics* (London, Wiley-Interscience, 1975).
- S9. Bliokh, K.Y. & Nori, F. Transverse spin of a surface polariton. *Phys. Rev. A* **85**, 061801(R) (2012).
- S10. Petersen, J., Volz, J. & Rauschenbeutel, A. Chiral nanophotonic waveguide interface based on spin-orbit interaction of light. *Science* **346**, 67–71 (2014).
- S11. O'Connor, D., Ginzburg, P., Rodriguez-Fortuno, F.J., Wurtz, G.A. & Zayats, A.V. Spin-orbit coupling in surface plasmon scattering by nanostructures. *Nature Commun.* **5**, 5327 (2014).
- S12. Bliokh, K.Y., Smirnova, D. & Nori, F. Quantum spin Hall effect of light. *Science* **348**, 1448 (2015).
- S13. Aiello, A., Banzer, P., Neugebauer, M. & Leuchs, G. From transverse angular momentum to photonic wheels. *Nature Photon.* **9**, 789–795 (2015).
- S14. Bohren, C.F. & Huffman, D.R. *Absorption and Scattering of Light by Small Particles* (Wiley, 1983).
- S15. Simpson, S.H. & Hanna, S. Orbital motion of optically trapped particles in Laguerre-Gaussian beams. *J. Opt. Soc. Am. A* **27**, 2061–2071 (2010).
- S16. Chaumet, P.C. & Nieto-Vesperinas, M. Time-averaged total force on a dipolar sphere in an electromagnetic field. *Opt. Lett.* **25**, 1065–1067 (2000).
- S17. Canaguier-Durand, A., Hutchison, J.A., Genet, C. & Ebbesen, T.W. Mechanical separation of chiral dipoles by chiral light. *New J. Phys.* **15**, 123037 (2013).
- S18. Wang, S.B. & Chan, C.T. Lateral optical force in chiral particles near a surface. *Nature Commun.* **5**, 3307 (2014).
- S19. Hayat, A., Mueller, J.P.B. & Capasso, F. Lateral chirality-sorting optical forces. *PNAS* **112**, 13190 (2015).
- S20. Tkachenko, G. & Brasselet, E. Spin controlled optical radiation pressure. *Phys. Rev. Lett.* **111**, 033605 (2013).
- S21. Tkachenko, G. & Brasselet, E. Optofluidic sorting of material chirality by chiral light. *Nature Commun.* **5**, 3577 (2014).
- S22. Cameron, R.P., Barnett, S.M. & Yao, A.M. Discriminatory optical force for chiral molecules. *New J. Phys.* **16**, 013020 (2014).
- S23. Draine, B.T. & Flatau, P.J. Discrete-dipole approximation for scattering calculations. *J. Opt. Soc. Am. A* **11**, 1491–1499 (1994).

- S24. Yurkin, M.A. & Hoekstra, A.G. The discrete-dipole-approximation code ADDA: capabilities and known limitations. *J. Quant. Spectrosc. Radiat. Transfer* **112**, 2234–2247 (2011).
- S25. Simpson, S.H. & Hanna, S. Application of the discrete dipole approximation to optical trapping calculations of inhomogeneous and anisotropic particles. *Opt. Express* **19**, 16526–16541 (2011).
- S26. Greenbaum, A. *Iterative Methods for Solving Linear Systems* (SIAM, 1997).
- S27. Goodman, J., Draine, B.T. & Flatau, P.J. Application of fast-Fourier-transform techniques to the discrete-dipole approximation. *Opt. Lett.* **16**, 1198–1200 (1991).
- S28. Chaumet, P.C., Rahmani, A., Sentenac, A. & Bryant, G.W. Efficient computation of optical forces with the coupled dipole method. *Phys. Rev. E* **72**, 046708 (2005).
- S29. Draine, B.T. & Weingartner, J.C. Radiative torques on interstellar grains: I. Superthermal spin-up. *Astrophys. J.* **470**, 551–565 (1996).
- S30. Gittes, F. & Schmidt, C.F. Thermal noise limitations on micromechanical experiments. *Eur. Biophys. J. Biophys. Lett.* **27**, 75–81 (1998).
- S31. Hutter, J.L. & Bechhoefer, J. Calibration of Atomic-Force Microscope Tips. *Rev. Sci. Instrum.* **64**, 3342–3342 (1993).
- S32. Evans, D.R., Tayati, P., An, H., Lam, P.K., Craig, V.S.J. & Senden, T.J. Laser Actuation of Cantilevers for Picometre Amplitude Dynamic Force Microscopy. *Sci. Rep.* **4**, 1–7 (2014).
- S33. Vassalli, M., Pini, V. & Tiribilli, B. Role of the driving laser position on atomic force microscopy cantilevers excited by photothermal and radiation pressure effects. *Appl. Phys. Lett.* **97**, 143105 (2010).
- S34. Höpfl, T., Sander, D. & Kirschner, J. Demonstration of different bending profiles of a cantilever caused by a torque or a force. *Am. J. Phys.* **69**, 1113–1115 (2001).